Available online at www.sciencedirect.com
SCIENCE DIRECT®
Journal of Power Sources 115 (2003) 323–331
JOURNAL OF POWER SOURCES
www.elsevier.com/locate/jpowsour

To the electrochemistry of pyrite in Li/solid composite-polymer-electrolyte battery

E. Strauss[a], D. Golodnitsky[a,b,*], K. Freedman[a], A. Milner[b], E. Peled[a]

[a]*School of Chemistry, Sackler Faculty of Exact Sciences, Tel Aviv University, Tel Aviv 69978, Israel*
[b]*Wolfson Applied Materials Research Center, Tel Aviv University, Tel Aviv 69978, Israel*

Received 14 October 2002; accepted 16 December 2002

Abstract

The purpose of this work is the study of the charge–discharge mechanism in the all-solid-state lithium/composite-polymer-electrolyte/pyrite battery operating at 120 °C. Effects on the charge–discharge mechanism of particle size, type of binder and cathode preparation method of the pyrite-based cathode are addressed. Analysis of the experimental XRD, XPS and electrochemical data suggests that creation of sulfur vacancies in pyrite suppresses a sudden jump of charge voltage, which is associated with slow mass transport of iron(II) cations through the Li_2FeS_2 phase. We believe that our experimental findings show considerable promise of creating sulfur-deficient pyrite structures for cathodes to be used in high-energy-density all-solid-state lithium batteries. The nature and exact composition of a 1.2–1.3 V discharge plateau is still unclear. To clarify the composition of this low-voltage phase synchrotron X-ray absorption measurements were performed on a series of cells cycled more than 100 times. The results will be presented in a forthcoming publication.

Keywords: Pyrite; Battery; Polymer electrolyte

1. Introduction

Iron sulfide (FeS_2) has been investigated as a positive electrode material in thermal, nonaqueous and polymer-electrolyte lithium batteries and several charge–discharge mechanisms have been discussed. In nonaqueous and molten media as well as in polymer electrolytes the discharge of FeS_2 was thought to proceed as a multi-stage process with the formation of metallic iron and lithium sulfide as the final discharge products. The $Li_3Fe_2S_4$, $Li_{11}Fe_4S_{10}$ and Li_2FeS_2 intermediates were detected on reversible charge–discharge of high-temperature (450 °C) pyrite cells with LiCl/KCl eutectic molten electrolytes [1,2]. For the Li/pyrite system in nonaqueous electrolyte the formation of Li_3FeS_4 [3], Li_2FeS_2 [4,5] or FeS [6] during discharge was suggested. It has been shown [7–9] that Li_2FeS_2 can be de-intercalated during charge with the formation of $Fe^{3+}(S_2^{2-})_{1/2}\,S^{2-}$ final structure. All the room-temperature cells showed extremely poor reversibility or none at all [3–6,10].

Good reversibility of Li/composite-polymer-electrolyte (CPE)/FeS_2 cells was obtained over the temperature range of 90–135 °C in [11]. From the analysis of dQ/dV curves [12] and EXAFS and NEXAFS tests [13] it was deduced that the reduction of ferrous disulfide proceeds as a multi-stage process via Li_2FeS_2 to metallic iron. No evidence of FeS was found. Two distinctive features characterize the reversible reduction of pyrite in composite-polymer-electrolyte. The first is a sudden voltage jump at about 1.85 V, that occurs on charging. The second is the appearance of a low-voltage 1.3 V plateau and the progressive increase of its contribution to the overall charge–discharge process. This is followed by a decrease in the specific energy of the battery. Several attempts were made to explain these phenomena [12–14], however, there is much still to be learned.

In this work, elucidation of the charge–discharge mechanism in the Li/(CPE)/FeS_2 battery has continued. In order to clarify the redox and insertion kinetics of pyrite and to estimate the compatibility of FeS_2 reduction products and CPE, three types of cathodes were tested: composite CPE-bonded cathodes prepared by casting and doctor blade methods, Teflon-bonded cathodes and 100% dense (composed of the active material alone) pure pyrite.

2. Experimental

The electrochemical cells studied comprise a lithium anode, $LiI_1P(EO)_{20}EC_1$ 12% by volume (v/v) Al_2O_3

* Corresponding author. Tel.: +972-3-640-6879; fax: +972-3-640-9293.
E-mail address: golod@post.tau.ac.il (D. Golodnitsky).

0378-7753/03/$ – see front matter © 2003 Elsevier Science B.V. All rights reserved.
doi:10.1016/S0378-7753(03)00013-2

composite-polymer-electrolyte and a 35–100% (v/v) pyrite-based cathode. The electrolytes were prepared from poly-(ethylene oxide) (P(EO)) (Aldrich, average molecular weight 5×10^6), which had been vacuum dried at 45–50 °C for about 24 h. The LiI (Aldrich) was vacuum dried at 150 °C for about 8 h. All subsequent handling of these materials took place under an argon atmosphere in a VAC glove box containing less than 10 ppm water. The detailed procedure of the polymer electrolyte preparation has been described elsewhere [11–13].

In our previous studies the 10–15 μm-thick cathode foil was prepared by dispersing fine natural pyrite powder (Chemalloy less than 10 μm size particles) in a polymer electrolyte slurry and cast on a Teflon tray. Grinding of pre-dried pyrite was performed in a hermetically sealed ball mill for 48 h. On casting of the composite cathode, FeS_2 tends to settle to the bottom, as its density is twice as that of the PE. The distribution of pyrite over the thickness of the cast cathode is, therefore, nonhomogeneous (Fig. 1a).

We addressed the problem in two ways. In the first stage of our work an effort was made to adapt the doctor blade (DB) technique, which is a commonly used method for the preparation of homogeneous battery cathodes, to the fabrication of thin-film pyrite-based composite cathodes. Composite cathodes were prepared by the addition of 35–80% (v/v) pyrite to a CPE or a mixture of 10% (v/v) Teflon and 5% (v/v) SiO_2 in cyclopentanone. The blended paste was poured on the graph foil and spread uniformly using doctor blade (DB). Composite cathodes were dried in vacuum at 70 °C for 8 h. As can be seen from the SEM micrographs (Fig. 1b) the pyrite is homogeneously distributed in the CPE network of the DB-cathode. The exfoliation of the graph foil, seen in the lower part of this image, is caused by quenching in liquid nitrogen, which was used for cross-section cutting of the cathode.

The second approach was directed towards the development of the procedure of RF sputtering (RFS) of ultra-thin 100% dense cathodes. Cycling of such cathodes allows rapid characterization of the performance of battery components. Such cathodes can be used in microbatteries as well. Ultra-thin (about 1 μm-thick) cathodes were prepared by RF sputtering (RFS) a pyrite target with the use of a Pfeiffer

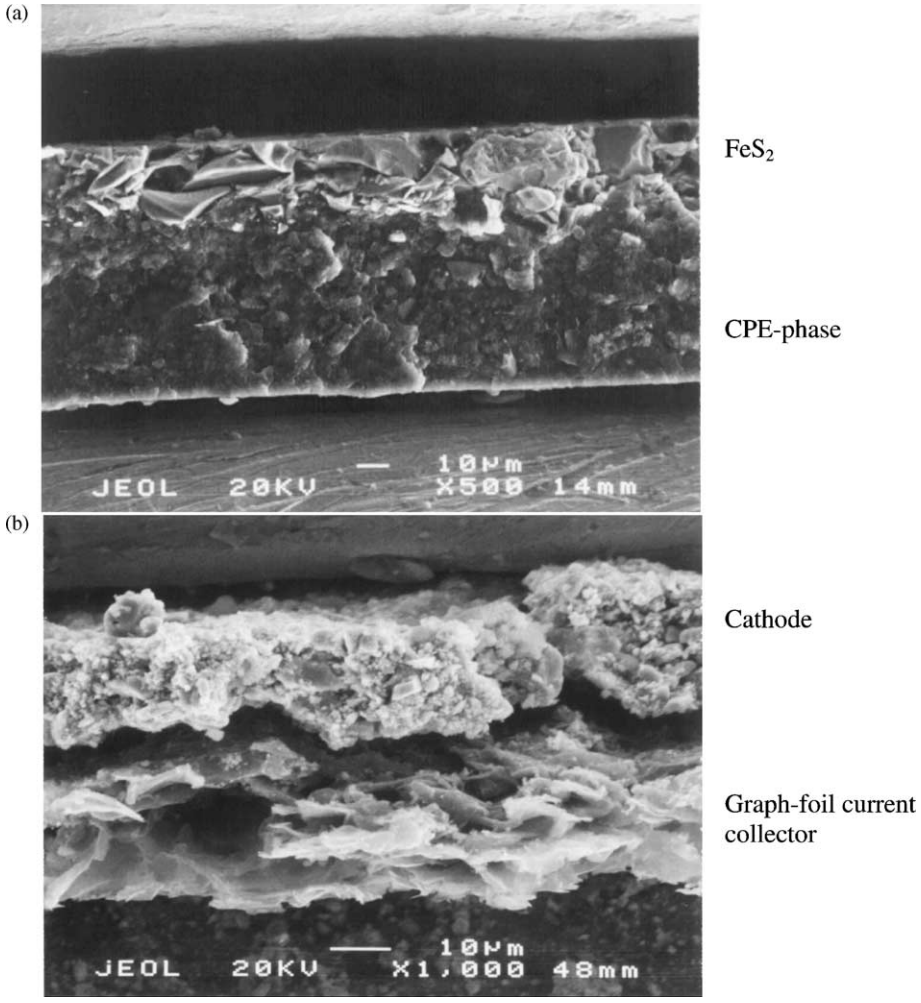

Fig. 1. SEM images of cross-section of as-cast composite cathode before hot pressing (a) and DB-cathode on graph foil (b).

vacuum PLS 160 instrument. RF power was 25 W, pressure 5×10^{-7} Torr, time of sputtering 6 h. The thickness of the 100% dense cathode, as measured by a profilometer was about 9000 ± 50 Å.

Carefully following all the steps of cathode preparation, we succeeded in obtaining reproducibility of battery performance (utilization of cathode active material, reversible capacity, charge–discharge overpotential) in the range of 2–5%.

The 0.95 cm^2 cells composed of a lithium anode, a 100–150 μm CPE film and a composite cathode were held under spring pressure inside a coin cell. Before each experiment, cells were equilibrated at 120 °C for at least 3 h. The batteries were cycled in a Maccor series 2000 battery test system.

A JSM-6300 scanning microscope (Jeol Co.) equipped with a Link elemental analyzer and a silicon detector was used to study surface topology. X-ray diffraction data were obtained with the use of a Θ–Θ Scintag powder diffractometer equipped with a Cu Kα source and a liquid-nitrogen germanium solid-state detector.

X-ray photoelectron (XPS) measurements of the pyrite cathodes were performed with a monochromatic Al Kα source (1486.6 eV) in UHV (2.5×10^{-10} Torr pressure) with the use of a 5600 Multi-Technique System (Physical Electronics Inc., USA).

3. Results and discussion

Fig. 2 shows the SEM surface images (in the secondary electrons mode) of the cathodes prepared by doctor blade technique (a, b) and RF sputtering (c, d). 1–10 μm size particles have been distinguished on the surface of the composite cathode, while nanosize pyrite particles were found in the RFS (100% dense) cathode. Topography images (obtained in the backscattering electrons mode) show full coverage of the surface of the current collector by pyrite for the cathodes prepared by both methods. Energy-dispersive X-ray analysis of the pyrite RF-sputtered cathode gives an Fe:S atomic concentration ratio close to 1:2, characteristic of pyrite FeS_2 structure.

In order to get more precise information on the composition of the RFS cathode, high-resolution XPS measurements were performed in the narrow window of 11.75 eV with 0.05 eV/step. The iron-binding energy (Fe 2p) region of the XPS spectrum of pyrite is shown in Fig. 3a. Two clear Fe 2p peaks at 720 and 706 eV characteristic of pyrite [14] and a broad peak at about 711 eV of iron oxides and/or iron sulfates are detected. This peak, in addition, may also include the compound FeOOH with binding energy 711.3–711.8 eV [14]. The oxygen O 1s signal at 532 eV is typical of iron oxides (Fig. 3b). The clear sulfur doublet at 162.4 and 163.6 eV in the S 2p-XPS spectrum is

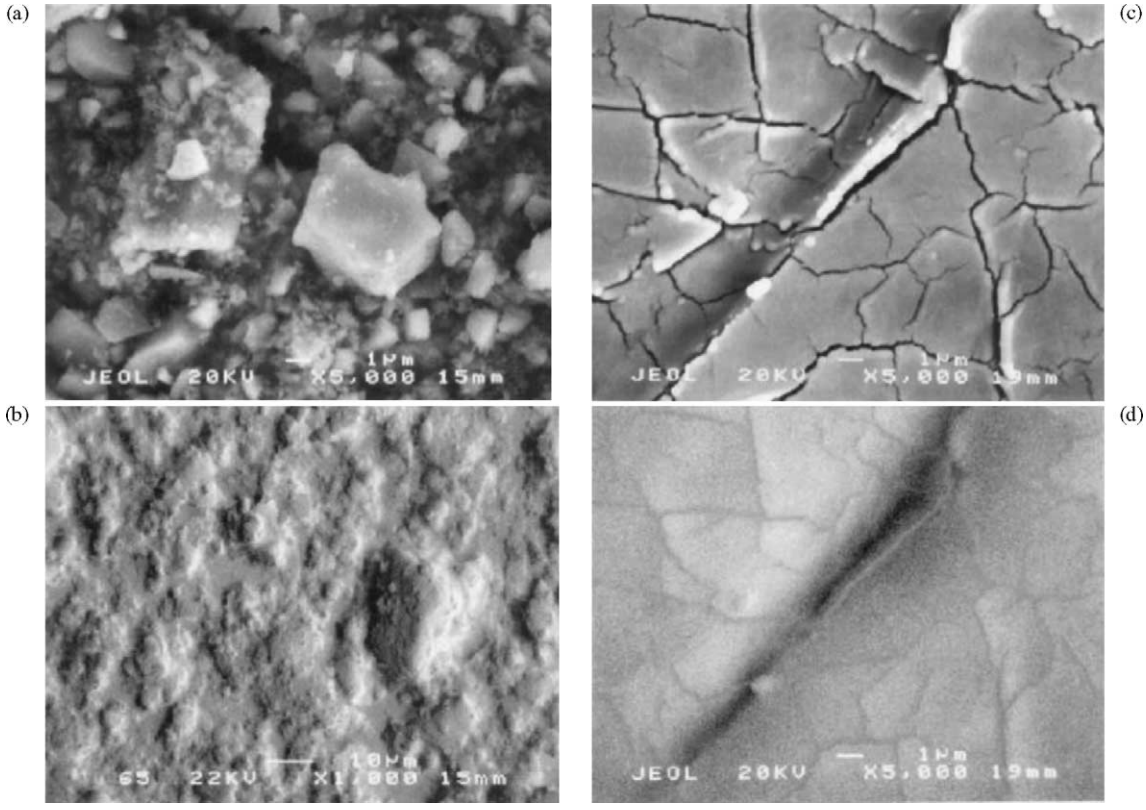

Fig. 2. SEM images of the surface of cathodes prepared by doctor blade technique (a, b) and RF sputtering (c, d): (a, c) secondary electrons mode; (b, d) backscattering electrons mode.

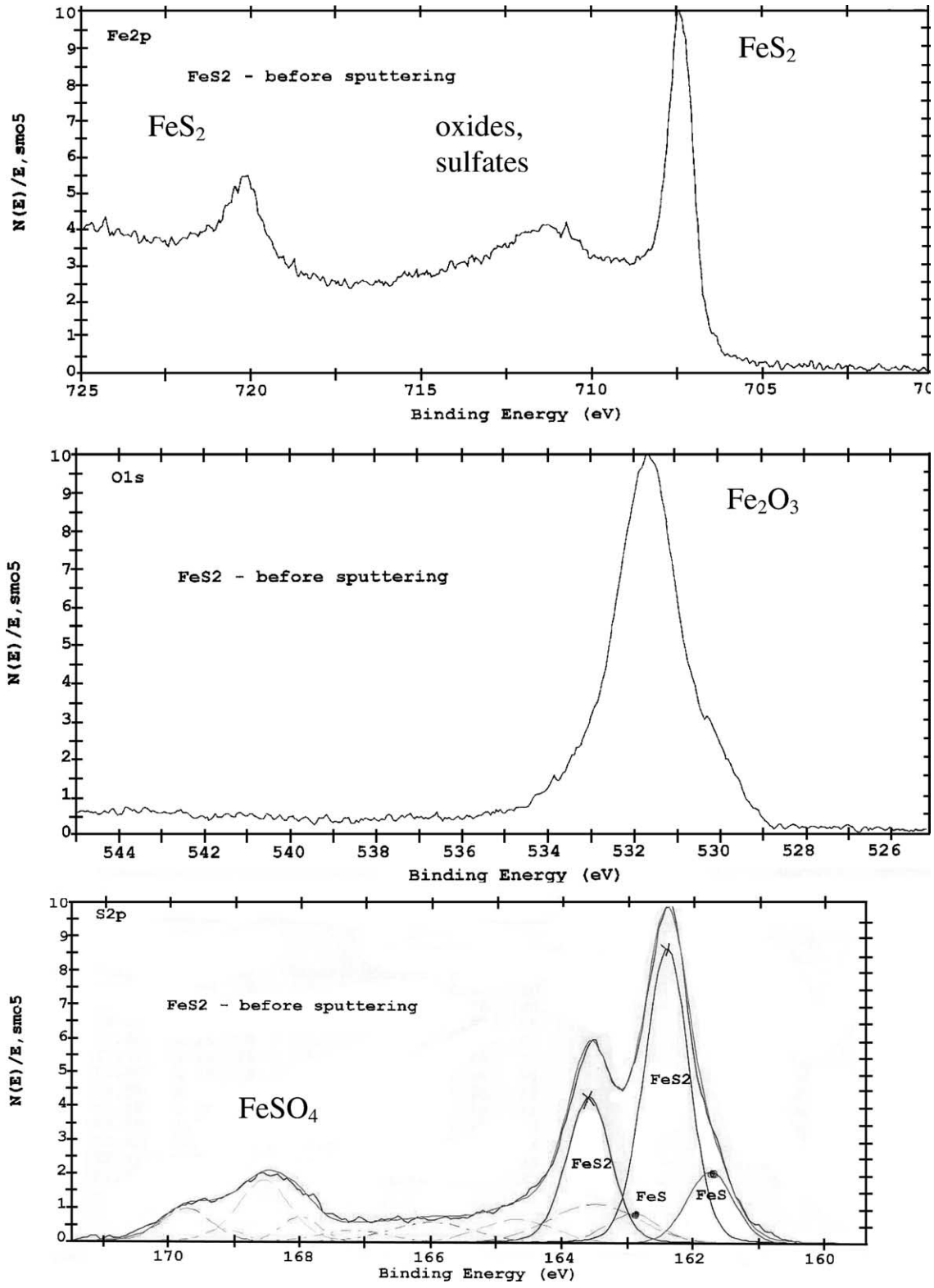

Fig. 3. High-resolution XPS spectra of the RFS-pyrite cathode.

related to pyrite, and the peak at 169 eV is attributed to the iron sulfates $Fe_2(SO_4)_3$ or $FeSO_4$ (Fig. 3c). It should be mentioned that there are no XPS standards that enable the identification of sulfur deficiency in pyrite. Fitting of the S 2p XPS spectrum was undertaken, therefore, with the use of the binding energy of FeS_2 and FeS (161.6 eV). As a result, about 20 at.% sulfur deficiency in pyrite was found. This presumably can be related to the

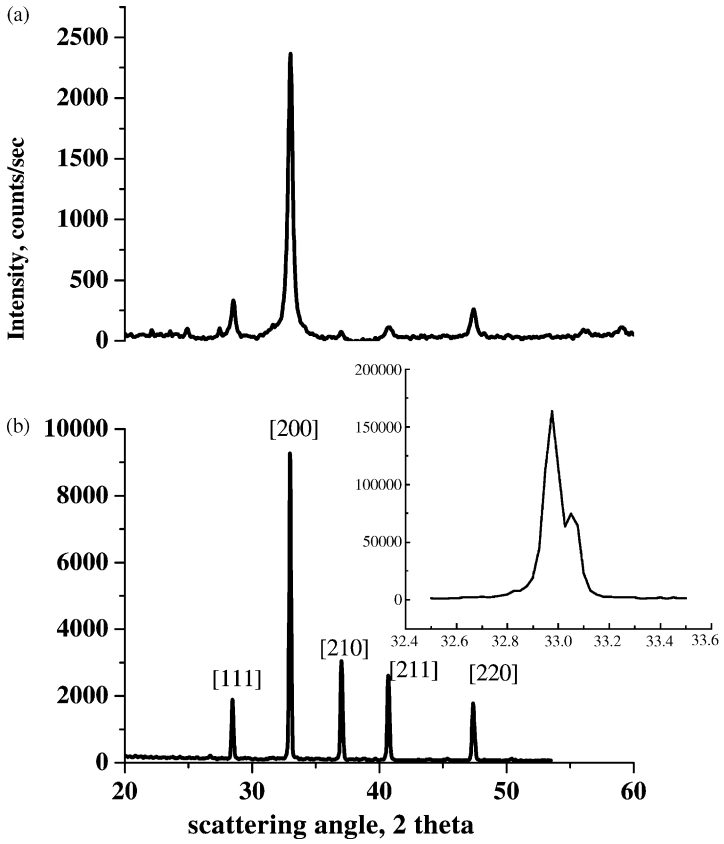

Fig. 4. XRD patterns of the RFS pyrite (a) and milled target (b).

formation of either $0.8FeS_2/0.2FeS$ mixture, or $FeS_{1.8}$ (Fe_5S_9) structure.

After 2 min of argon sputtering, the relative atomic concentration of oxygen strongly decreases, indicating the absence of oxides in the bulk of the RFS cathode. The Fe:S atomic ratio does not change even after 10 min of sputtering. This points to the formation of a homogeneous sulfur-deficient structure in the RFS cathode.

As expected, the substrate on which sputtering is performed, influences the final structure of the material. Pyrite sputtered on glass (Fig. 4a) is much more oriented than natural FeS_2 powder (Fig. 4b). A high-intensive [2 0 0] peak indicates formation of a strong texture with about 10–20 nm grain size. This texture, while strong enough, is less pronounced when sputtering is performed on a graph foil current collector. In the XRD pattern of the FeS_2-RF sputtered cathode both on the glass and graph foil, the main Bragg lines associated with pyrite were detected. In the pristine FeS_2 each iron atom is coordinated by six sulfur atoms, while sulfur has bonds with three Fe and one S [15,16]. The iron atoms are arranged in the face-centered cubic (fcc) sublattice in which the S atoms are imbedded. The RFS pyrite was found to have an increased lattice parameter (5.4365 Å) as compared to that of powder obtained by milling of the target (5.4167 Å). This enlargement of the cell unit is not clear enough. It is assumed that RF sputtering is followed by the creation of sulfur defects and conversion of the octahedral sulfur arrangement to a disturbed tetragonal pyramidal symmetry with the FeS_5 molecule. In this coordination the d_{xz}, d_{xy} and d_{yz} orbitals are energetically more stabilized [15,16], thus resulting in an additional state in the forbidden zone as a result of the sulfur deficit. In [15,16] it was found that, even for the case of only 5% (atomic) sulfur deficiency, approximately 25% of the iron coordination would be affected as well. For about 20% sulfur deficiency, as in RFS pyrite, almost all the iron atoms would be disturbed. Therefore, by analogy with [15,16], the electron conductivity of the RFS pyrite is expected, therefore, to be higher than that of the pristine material.

More than 50 cells with pyrite-based cathodes of different active-material content and thickness were constructed and cycled. Fig. 5 represents the first discharge curve of Li/CPE/pyrite cells with cathodes prepared by DB and RFS. For a Li/(CPE)/FeS_2 cell, the first discharge curve at 120 °C has two plateaus, one at about 1.8 V and another at 1.6 V. These are associated with the two-step reduction of FeS_2 (according to reactions 1 and 2):

$$FeS_2 + 2Li^+ + 2e \rightarrow Li_2FeS_2 \quad (1)$$

$$Li_2FeS_2 + 2Li^+ + 2e \rightarrow Fe + 2Li_2S \quad (2)$$

The high-voltage (2.4–1.8 V) shoulder appearing on the discharge curve may be attributed to the reduction of the partially oxidized cathode surface. This shoulder is more

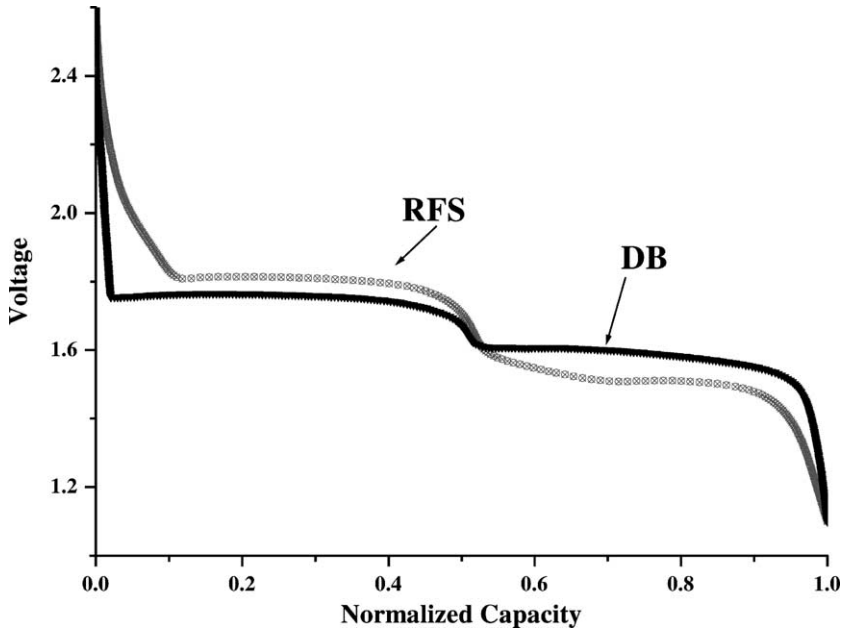

Fig. 5. First discharge of the Li/CPE/FeS_2 cells. CPE composition: LiI $P(EO)_{20}$ EC_1, 9% Al_2O_3; operating conditions: $T = 120\ ^\circ C$, $i_d = 0.05\ mA/cm^2$; cathode composition: DB, 50% (v/v) FeS_2, 50% (v/v) CPE; cathode thickness, $\delta = 10\ \mu m$; RFS, 100% FeS_2, $\delta = 1\ \mu m$.

pronounced on discharge of the nano-size, roughly 1 μm-thick RF-sputtered cathode. The overpotential of the first step of pyrite reduction is lower by 50 mV for the RF-sputtered cathodes. However, it is higher by 75 mV for the second step. This difference may indicate that Li^+ mobility is hampered in the Li_2FeS_2 phase in the absence of the CPE in the 100% dense cathode.

The first-cycle utilization of pyrite was found generally to be inversely proportional to the thickness of the DB-composite cathode and pyrite content. At low FeS_2 content (35%) the effect of thickness is less pronounced. Hot-pressing of cathodes results in a rise of FeS_2 utilization by 6–18%. Teflon-bonded cathodes showed 50% pyrite utilization. Utilization of pyrite during the first discharge in the ultra-thin RF sputtered cathodes was the highest (88%).

Over the operating temperature of 120 °C, pyrite is not regenerated on charge, therefore, the discharge curves from the second cycle on differ from that of the first cycle. The simplified charge–discharge mechanism of pyrite in polymer electrolytes has been studied extensively [9,11–13,17,18] and may be schematically described by the following reactions:

$$Fe + 2Li_2S - 2e \rightarrow Li_2FeS_2 + 2Li^+ \quad (3)$$

$$Li_2FeS_2 - XLi^+ - Xe \rightarrow Li_{2-X}FeS_2 \quad (0.5 < X < 0.8) \quad (4)$$

To get more precise information on the small changes occurring during charge–discharge, we carried out high-resolution voltage measurements. Four to seven phases have been identified and found to change during the first 30–50 cycles. These phases do not change much over the subsequent 400–500 cycles. (Fig. 6) depicts the dQ/dV curves of the second charge–discharge cycle of cells composed of pyrite-based RFS and DB-composite cathodes. On the basis of on our previous studies, we associate peaks B and C with reversible electrochemical reaction 3. The flat, high-voltage sections of the curves (1.9–2.2 V on charge and 1.75–2.1 on discharge) are attributed to the reversible insertion/deinsertion of lithium to/from the Li_2FeS_2 host, complicated by a phase change (peaks D and A). This phase transition is more pronounced in the case of cathodes composed of natural pyrite. Deinsertion of lithium results in the oxidation of iron(II)–(III), the process being accompanied by a change in iron-ion occupancy from tetra- to octahedral at an advanced stage of the reaction [7,19]. Peak D, therefore, is likely to be related to the shift of iron atoms from tetra- to octahedral coordination. It has been recently found [17,20] that pyrolysis of pyrite is followed by a 100 mV decrease in the charge overpotential. This was explained by the formation of tetrahedral sulfur vacancies in the Li_2FeS_2 phase, which may be occupied by iron ions. Strong depression of peak D in the dQ/dV curves of the lithium cells with RFS-cathodes may be, therefore, related to the formation of a sulfur-vacancy-rich structure, similar to that formed on pyrolysis. This structure has increased lattice space detected by XRD and XPS methods. This is in agreement with data presented by Blandeau et al. [19], who showed that in Li_2FeS_2 the Fe–S interatomic distance for the main (FeS_4) tetrahedra is 2.357 Å. For the surrounding octahedra the Fe–S distance is 2.53 Å. Such structure is expected to permit greater mobility of iron, which, in turn, favors the tetra- to octahedral iron shift. In addition, a low S/Fe ratio in the FeS_2 lattice was followed by enhanced electron conductivity of the material [21], thus decreasing the IR drop and probably increasing diffusion coefficients of

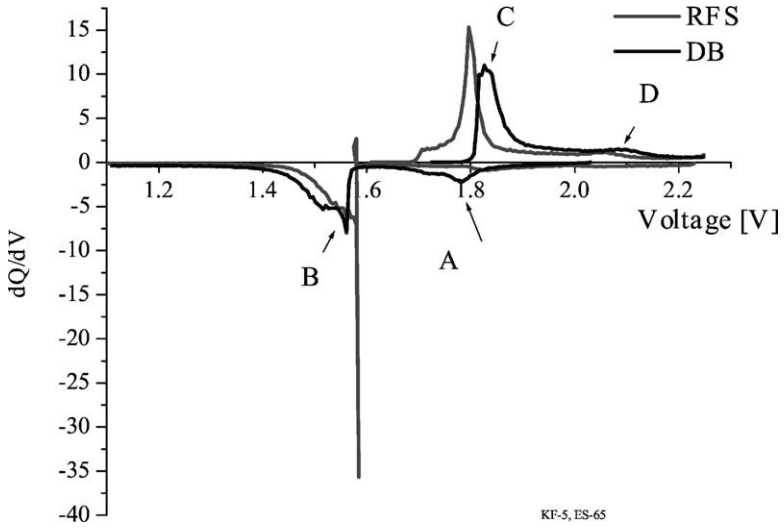

Fig. 6. dQ/dV curves of the of the second cycle of the Li/CPE/FeS_2 cells with RFS and DB cathodes. Operating conditions: $T = 125$ °C, $i_d = i_{ch} = 0.05$ mA/cm^2.

Li^+, Fe^{2+} and Fe^{3+}. Low charge/discharge overpotential of the lithium cells with RFS cathodes (Fig. 6) is good evidence of increased electronic conductivity of the sputtered pyrite.

Fig. 7 shows dQ/dV curves of long-term cycling of the Li/CPE/FeS_2 cells with different cathodes. In the cells with both RFS, cast and DB composite pyrite CPE-bonded cathodes, the maximum of the discharge peak B shifts to lower cell voltages by about 40 mV. Also, on further cycling up to about cycles 20–30 an additional shoulder develops. The amount of the generated phase increases, but the position of the peak does not change much over the subsequent 100 cycles, indicating the attainment of the phase steady state in the cathode. At high discharge current density (300 μA/cm^2, c/3) peak B in the discharge curves of the cells with composite cathodes gradually shifts toward low voltage by 70–100 mV. We believe that this phenomenon may be due to the transport limitations of Fe^{2+} in Li_2FeS_2 followed by the occurrence of an ion-transport barrier similar to that of the limiting current phenomenon. For RFS cathodes, however, increase of the discharge rate from c/7.5 to c/1.8 does not affect the long-term discharge overpotential.

Long-term cycling of the cells with Teflon-bonded cathodes (Fig. 7d) is followed by intensive build-up of discharge overpotential. This is possibly due to the increased mass-transport limitations and the IR drop as a result of negligible Li^+ conductivity of Teflon and loss of contact between active cathode material particles. At the end of the second and all subsequent discharges, the fractional change in the cathode active material volume is about +27%. On charge, the cathode contracts by about 21% [12]. It seems likely that the Teflon used as a binder in composite pyrite-based cathodes does not sufficiently prevent the separation of cathode-active material particles.

At deep discharge (down to 1.1 V) of lithium/composite-polymer-electrolyte/pyrite battery an additional plateau forms at about 1.3 V. It is noteworthy that in the dQ/dV curves of the Li/FeS_2 cells with cast cathodes this plateau appears as a pronounced peak (Fig. 7b); for the cathodes prepared by the DB technique, the increased contribution of low-voltage reactions emerges as progressively increased area below the zero dQ/dV level (Fig. 7c). In our previous work [12], we suggested that several parallel, undesirable reactions might take place resulting in the formation of an additional phase. It is now well established by powder X-ray diffraction (PXRD), near-edge X-ray absorption spectroscopy (NEXAS) and Mossbauer spectroscopy [10,18,22,23], that the final product of fully reduced pyrite is supermagnetic iron in the form of atoms or small (about 3.6 nm) aggregates of atoms. These are highly active and have a large surface area. Such a cathode surface becomes highly susceptible to attack by the electrolyte components, which comprise 20–65% (v/v) of the composite cathode. Partial decomposition of the electrolyte and the formation of undesirable products bear out the electrochemical incompatibility of nanosize iron particles and CPE. Although the electrochemical reactions are reversible, they decrease the total operating voltage and increase capacity loss of the battery. The low-voltage plateau appearing as a broad peak in the high-resolution dQ/dV discharge curves of the Li/pyrite cells with RFS cathodes (Fig. 7a) is scarcely visible even in enlarged 1.1–1.5 V region. However, the graduate development of the 1.6 V shoulder on charge may indicate that, while less pronounced, there is the formation of the low-voltage phase. The absence of the CPE as binder in the RFS cathode may explain depression of the dQ/dV peak at 1.2–1.3 V. Therefore, the high reactivity of nanosize iron particles towards CPE can not be excluded. To clarify the composition of the 1.3 V phase synchrotron X-ray absorption measurements were performed on a series of cells cycled more than 100 times. The results will be presented in a forthcoming publication.

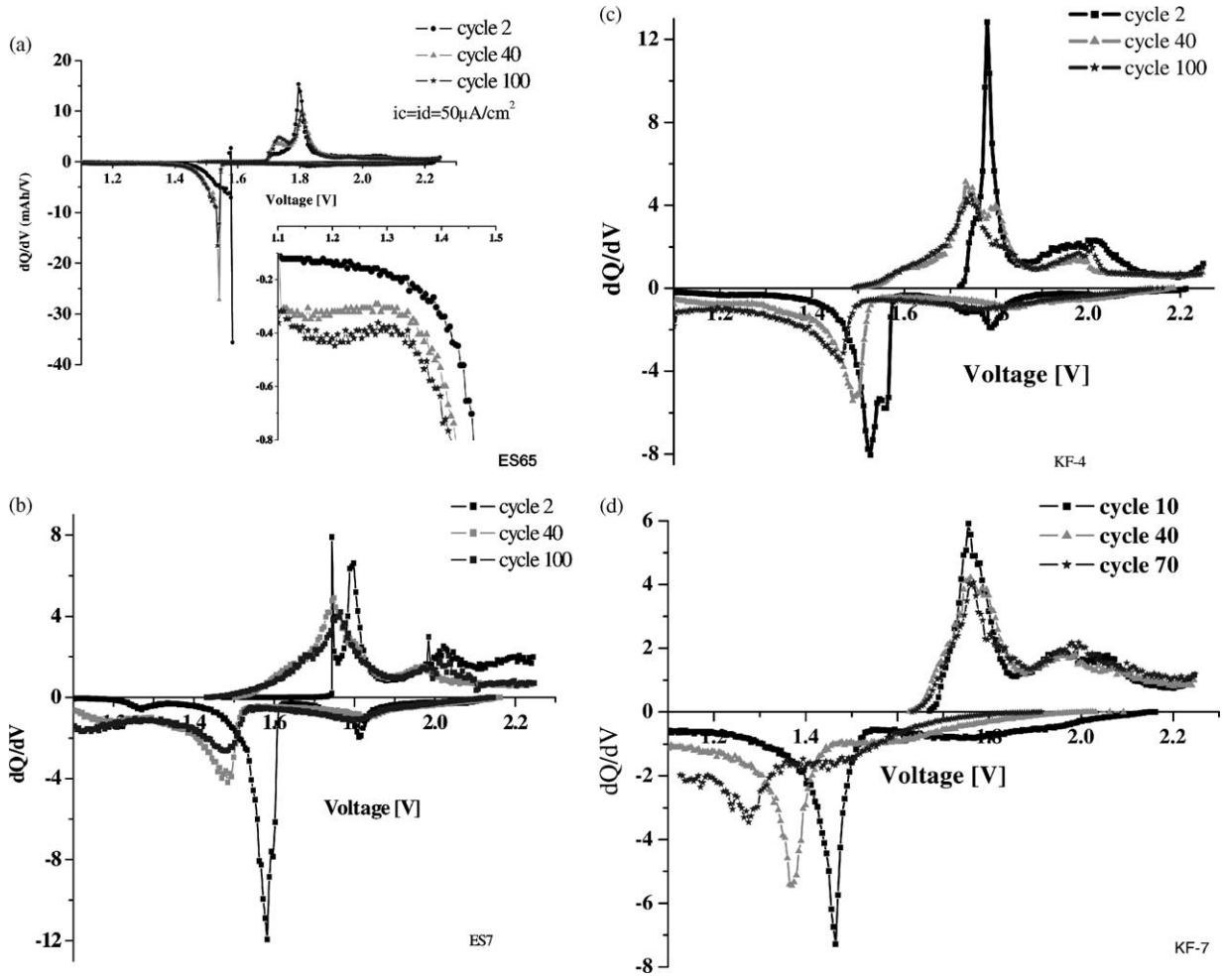

Fig. 7. dQ/dV curves of the long-term cycling of the Li/CPE/FeS_2 cells with different cathodes: (a) RFS*; (b) CPE-bonded cast; (c) CPE-bonded DB; (d) Teflon-bonded DB. Operating conditions: $T = 125$ °C, $i_d = 0.05$ mA/cm^2, $i_{ch} = 0.3$ mA/cm^2. (∗) $i_d = i_{ch} = 0.05$ mA/cm^2.

Fig. 8 shows the plots of capacity loss and charging efficiency of the Li/CPE/pyrite cells with RFS- and DB-cathodes. It is clear that the main capacity loss of all the cells occurs during the first 30 cycles (0.4–0.5% per cycle). On subsequent cycling, the degree of degradation decreases to 0.1–0.15% per cycle. The Faradaic efficiency increases, respectively, from 90 to 96%. This coincides with an attainment of the phase steady state in the cathode. The capacity loss in the cells with cast, DB and CPE-bonded composite cathodes and Teflon-bonded cathodes is 0.2–0.4% per cycle at $i_d = 300$ μA/cm^2 (c/3.3) and $i_c = 50$ μA/cm^2 (c/20).

In order to prevent undesirable reactions occurring at deep discharge and to achieve long-term stability of the CPE-containing composite cathodes (similar to that of the Li/FeS_2 cells with RFS cathodes), the procedure of the formation of cathode SEI was developed [12,24]. This is based on the overdischarging of the Li/FeS_2 cells during several cycles. The cathode SEI increases compatibility of the CPE with atomic iron and, as a result, decreases the long-term degree of degradation of the Li/CPE/pyrite cells to 0.1% per cycle.

We would like to emphasize that there is almost no change in the capacity loss with increase in charge–current density up to c/1.8 in Li/CPE/pyrite cells with RFS cathodes. For the cells with cathode composed of natural pyrite and bonded with CPE the degradation rate for the same operating conditions increases up to 0.5–0.8% per cycle. We believe

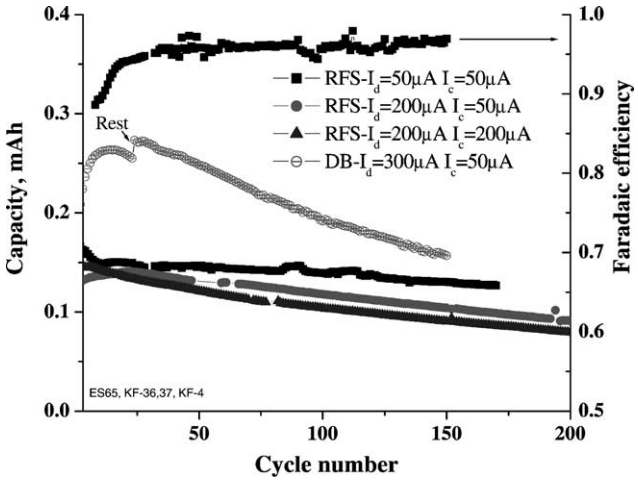

Fig. 8. Plots of discharge capacity and Faradaic efficiency vs. cycle number.

that our experimental findings show considerable promise of creating sulfur-deficient pyrite structures for cathodes to be used in high-energy-density all-solid-state lithium batteries.

3.1. Summary

Characterization of three types of FeS_2-cathodes for Li/CPE/pyrite battery was obtained by SEM, XPS, XRD, and electrochemical methods. Analysis of the experimental data, suggests that it is the mass transport of iron cations through the Li_2FeS_2 that slows the charge rate and creates a charge overvoltage. Formation of sulfur vacancy-rich pyrite structure eliminates transport limitations of iron in Li_2FeS_2 and shows promise for the design of cathodes for high-energy-density lithium batteries.

The nature and exact composition of a low-voltage 1.2–1.3 V discharge plateau is still unclear. It may be possibly attributed to a reaction of metallic iron with polymer electrolyte filling the pores of the composite cathode. Formation of cathode SEI prevents undesirable reactions from occurring at deep discharge and increases the long-term stability of the Li/FeS_2 cells.

Acknowledgements

We would like to thank the Government of Israel and USAF for financial support. We thank to Dr. Yu. Rosenberg and Dr. L. Burstein from Wolfson Applied Materials Research Center of Tel Aviv University for conducting XRD and XPS measurements.

References

[1] L. Gary, Henriksen, Lithium/iron sulfide batteries, in: Handbook of Batteries, 1995, pp. 39.1–39.17.
[2] Z. Tomczuk, B. Tani, N.C. Otto, M.F. Roche, D.R. Vissers, J. Electrochem. Soc. 129 (1982) 926.
[3] J.C. Nardi, M.B. Clark, W.P. Evans, in: Proceedings of the Symposium on Electric Power Sources in Horological and Microtechnical Protection, Mulhause, France, Extended Abstracts, 1981, p. 48.
[4] C. Iwakura, N. Isobe, H. Tamura, Electrochim. Acta 277 (1983) 126.
[5] H. Ikeda, S. Narukawa, S. Nakaido, in: Proceedings of the 21st Battery Symposium in Japan, Okayama, Extended Abstracts, 1980, p. 47.
[6] K. Hansen, K. West, Electrochem. Soc. Proc. 18–97 (1997) 124.
[7] R. Brec, E. Prouzet, G. Ouvrard, J. Power Sources 26 (1989) 325.
[8] P. Gard, C. Sourisseau, G. Ouvrard, R. Brec, Solid State Ion. 20 (1986) 231.
[9] D.A. Scherson, Electrochem. Soc. Interf. Fall (1996) 34.
[10] R. Fong, J.R. Dahn, C.H.W. Jones, J. Electrochem. Soc. 136 (11) (1989) 3206.
[11] E. Peled, D. Golodnitsky, G. Ardel, J. Lang, Y. Lavi, J. Power Sources 54 (1995) 496.
[12] E. Strauss, D. Golodnitsky, E. Peled, Electrochim. Acta 45 (8–9) (2000) 1519.
[13] E. Strauss, D. Golodnitsky, E. Peled, S. Kostov, D. Garan, M. denBoer, S. Greenbaum, J. Power Sources 81–82 (1999) 715.
[14] J. Chastain (Ed.), Handbook of X-Ray Photoelectron Spectroscopy, Perkin-Elmer, USA, 1992.
[15] A. Ennaoui, S. Fiechter, Ch. Pettenkofer, N. Alonso-Vante, K. Buker, M. Bronold, Ch. Hopfner, H. Tribusch, Solar Energy Mater. Solar Cells 29 (1993) 289.
[16] M. Birkholz, S. Fiechter, A. Hartmann, H. Tributsch, Phys. Rev. B 43 (14) (1991) 11926.
[17] E. Strauss, D. Golodnitsky, E. Peled, J. Solid State Electrochem. 6 (2002) 468–474.
[18] D.A. Totir, I.T. Bae, Y. Hu, Y. Gofer, Y. Mo, D.A. Scherson, Proc. Symp. Lithium Polym. Batt. 96–17 (1996) 269.
[19] L. Blandeau, G. Ouvrard, Y. Calage, R. Brec, J. Rouxel, J. Phys. C: Solid State Phys. 20 (27) (1987) 4271.
[20] D. Golodnitsky, E. Peled, Electrochim. Acta 1–2 (45) (1999) 335.
[21] C. de las Heras, G. Lifante, J. Appl. Phys. 82 (10) (1997) 5132.
[22] K. Takada, Y. Kitami, T. Inada, A. Kajiyama, M. Kouguchi, S. Kondo, M. Watanabe, M. Tabuchi, J. Electrochem. Soc. 148 (10) (2001) A1085–1090.
[23] D.A. Totir, M.R. Antonio, P. Schilling, R. Tittsworth, D.A. Scherson, Electrochim. Acta 47 (2002) 3195.
[24] E. Strauss, D. Golodnitsky, E. Peled, Electrochem. Solid State Lett. 2 (3) (1999) 115.